Analytical and Experimental Study of Multilayer Dielectric Rod Waveguides

Denise C. Lugo, *Member, IEEE*, Jing Wang, *Senior Member, IEEE* and Thomas M. Weller, *Fellow, IEEE*

Abstract— **This paper presents a comprehensive study of the design and performance of a multilayer dielectric rod waveguide (MDRW) with rectangular cross section. The design is comprised of a high permittivity core encased by a low permittivity cladding. A mathematical model is proposed to predict the fundamental mode cutoff frequency in terms of the core dimensions and the core and cladding permittivity. The model is useful for design purposes and it offers an excellent match to full-wave EM simulation results. The MDRW performance is measured for the extended Ku band (10-18 GHz) considering straight and bent waveguides with different radius of curvatures. The particular multilayer configuration shows a 16.7% and 24% extension of the 1 dB low-band cutoff frequency for a 10 × 10 mm² and 20 × 20 mm² cladding area, respectively, when compared to a single layer dielectric rod waveguide (DRW) design of the same core dimensions. MDRW bends also exhibit significant reduction of the 1 dB low-band cutoff frequency from 20% to 40% when compared to single layer designs, for different radius of curvature bends.**

Index Terms— **additive manufacturing, dielectric rod waveguide, Ku band, multilayer, rectangular waveguide.**

I. Introduction

THE continuous and systematic push of the Internet of Things (IoT) and 5G wireless protocols will require millimeter wave (mm-wave) systems that offer wide channel bandwidth and high power handling for successful data transmission to end users [1]. Thus, the implementation of low loss waveguide structures at mm-wave frequencies is of ever growing importance. Planar metal strip transmission lines, such as microstrip and coplanar waveguide (CPW) that are successfully used at microwave frequencies can exhibit high conductor and dielectric losses in the mm-wave frequency range [2]. Dielectric waveguides naturally eliminate conductor losses and have been successfully implemented in the mm-wave and THz regimes. High performance dielectric waveguides have been used for a wide variety of applications such as biomedical imaging [3], spectroscopy [4] and communication systems [5]. These waveguides are usually divided into three categories: hollow core, porous core and solid core [4]. Typically, the hollow core waveguides exhibit the lowest losses since most of the electromagnetic waves propagate through the hollow center of the guide [4]. But in order for this to occur, the core dimension has to be much larger than the wavelength and this can lead to narrow operational bandwidths or detrimental multimode propagation [4, 6]. Porous core waveguides are created by introducing a certain distribution of sub-wavelength air holes into the core of the dielectric structure. Some innovative geometric designs have been proposed in order to achieve low transmission loss and high mode confinement [7-10]. The main disadvantage of these designs is typically the fabrication complexity that depends on the distribution, shape and size of the air holes [4]. Among dielectric waveguides, the solid core designs introduce the higher dielectric absorption losses but their ease of fabrication, wide bandwidths and the possibility of planar implementation are attractive features. Some solid core waveguide designs such as dielectric ribbons are compatible with multilayered printed circuit boards (PCBs) [11] and on-wafer integration [12].

This work investigates the design and performance of multilayer dielectric rod waveguides with rectangular cross section. The proposed design is formed by a high permittivity rod surrounded by a low permittivity cladding. The low permittivity cladding is used to enhance the waveguide performance by increasing the bandwidth and reducing the losses in bends. This additional dielectric layer does not measurably increase the waveguide insertion loss since most of the electric field propagates in the waveguide core. The cladding also diminishes the possible electromagnetic interactions between the waveguide core and adjacent structures since the electric field is largely confined within the multilayer design. As shown in our prior work [13], this unique characteristic can be used to prevent degradation of the waveguide performance due to lossy substrates or neighboring waveguides.

In this work, the cladding is fabricated using a digital additive manufacturing (AM) technology called fused deposition modeling (FDM), which has been used for applications up through mm-wave frequencies [14, 15]. With FDM, structures are formed using a controlled layer-by-layer deposition of thermoplastics or thermoplastic composites. The layer height depends on the printing nozzle size and typically can range from

Manuscript submitted for revision on June 24, 2020. This work was supported by the National Science Foundation under Grant ECCS-1509762.

D. C. Lugo and J. Wang are with the University of South Florida, Tampa, FL 33620 USA (e-mail: deniselugo@mail.usf.edu; jingw@usf.edu).

T. Weller is with Oregon State University, Corvallis, OR 97330 USA (e-mail: tom.weller@oregonstate.edu).

300 µm down to 25 µm. Similar techniques have been used with success in the fabrication of other RF/microwave components [14, 15]. The AM approach is especially useful in this study as it provides a low cost means of experimentally validating different designs with a rapid turn-around time. In our prior work, a similar multilayer waveguide design was implemented for the Ku band and completely fabricated using FDM [16]. In that work, the cladding is made of acrylonitrile butadiene styrene (ABS) while the core is formed using an in-house custom developed ceramic composite.

In addition to experimental results, this paper presents a closed-form model for the MDRW that is instrumental for design purposes. It is well known that there is no analytical solution to the wave propagation problem in a rectangular rod, and this can make the analysis of rectangular dielectric rod waveguides tedious. Several approximation methods have been proposed in the literature to address this issue; two of the most popular were proposed by Marcatili [17] and Goell [18]. Marcatili's method is derived in the Cartesian coordinate system by considering the rod as a superposition of two dielectric slab waveguides and assuming well-confined modes. Goell solves the problem using a cylindrical coordinate system and proposes a solution based on a modified Bessel function multiplied by trigonometric functions. Herein, an explicit analytical model for the waveguide low-band cutoff frequency is proposed. The model predicts the appropriate waveguide dimensions for a given cutoff frequency, based on the material properties and operational frequency range.

The following section presents a study of the MDRW design guidelines and modal analysis. Section III proposes an explicit analytical model of the MDRW cutoff frequency as a function of the core dimensions as well as material properties of the core and cladding. Section IV presents a study of the cladding effect on the MDRW performance and Section V shows the characterization of the MDRW for the extended Ku band that was first described in [13]. Measured data of different straight and bent waveguides are presented and a breakdown of the losses versus frequency due to the dielectric material, transition and radiation is also included. The main contributions of this work on the study of dielectric rod waveguides are twofold: the derivation of an explicit analytical model for the MDRW cutoff frequency, and the experimental characterization of the cladding effect in MDRW under various conditions along with the estimation of loss sources.

II. Multilayer Dielectric Rod Waveguide (MDRW)

A. Design Considerations

The proposed MDRW design is comprised of a high dielectric constant core surrounded by a low dielectric constant cladding [13]. The core is a dielectric rod waveguide with rectangular cross section as illustrated in Fig. 1. In this work, the width of the core is optimized for the Ku band based on numerical simulation data obtained using high frequency structure simulator (HFSS) by Ansys. As a starting point for the optimization, the width of the core can be approximated to be the maximum thickness for a dielectric slab waveguide with single mode operation [19]:

$$\textit{Slab Thickness} \ < \frac{\lambda_0}{2} \frac{1}{\sqrt{n_{core}{}^2 - n_{clad}{}^2}} \tag{1}$$

where n_{core} and n_{clad} are the refractive indexes of the core and cladding, respectively.

In the MDRW, the guiding mechanism is total internal reflection and the modes it supports are hybrid and polarized in the x or y directions assuming propagation in the z direction. The guided modes in the MDRW belong to either the E^y_{nm} or E^x_{nm} families, where n and m are the number of maxima in the x and y directions, respectively, and the superscript x or y indicates the direction of the field polarization [20]. If the core refractive index is lower than that of the cladding, the guiding no longer occurs by the principle of total internal reflection but rather by photonic bandgap [4].

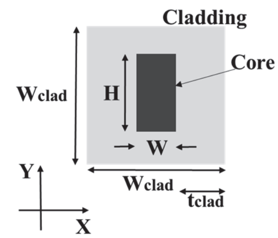

Fig.1. Multilayer dielectric rod waveguide cross-section and key parameters

The core cross-section dimensions and the refractive indexes of the core and cladding determine the MDRW mode cutoff frequencies. If n_{core} and n_{clad} are close in value, the largest field component is normal to the propagation direction in a TEM-like mode [17]. On the other hand, it has been demonstrated that if the refractive indexes of the core and cladding are so close that (2) is satisfied, it will cause the modes E^y_{mn} and E^x_{mn} to degenerate since the axial propagation constant and the penetration depth of both will be approximately the same [17].

$$\frac{1}{n_{core}}\left(n_{core} - n_{clad}\right) << 1 \tag{2}$$

A larger difference between the refractive indexes of the core and cladding will break field degeneracies depending on the core cross-section aspect ratio. Also, for a certain n_{core}, increasing the value of n_{clad} decreases the fundamental mode cutoff frequency as the effective core size increases. The cladding effect on the MDRW performance is discussed in more detail in Section II B.

Considering a certain field polarization, a square core cross section provides the largest single mode operation bandwidth, i.e. the largest difference between the fundamental E_{11} mode and the E_{21} mode [6]. When x and y field polarizations are both present in the square dielectric waveguide, due to symmetry, all the modes are degenerate even for larger differences between n_{core} and n_{clad}. In this case, a core cross-section aspect ratio different than 1:1 can break the field degeneracies, but as one dimension increases over the other the single mode operation bandwidth reduces [6].

Unlike metal waveguides, modes propagating in dielectric rod waveguides extend outside the waveguide geometry. The rod geometry, material properties and frequency determine the extent of field confinement inside the waveguide core. The DRW's normalized propagation constant is defined as:

$$P^2 = \frac{\left(K_z/K_{clad}\right)^2 - 1}{\left(K_{core}/K_{clad}\right)^2 - 1}, \qquad (3)$$

where K_z is the axial propagation constant, $K_{\text{core}}=\omega(\mu_0\varepsilon_{\text{core}})^{1/2}$ and $K_{\text{clad}}=\omega(\mu_0\varepsilon_{\text{clad}})^{1/2}$. The normalized propagation constant can vary for guided modes from 0, when the mode starts propagating and $K_z = K_{\text{clad}}$, to 1, when the mode is completely confined inside the core and $K_z = K_{\text{core}}$ [17].

Fig. 2 illustrates the HFSS simulated DRW fundamental mode electric field distribution for designs with different permittivity conditions. The normalized propagation constant is used in each case to quantify the field confinement. For these data, a DRW with a rectangular cross section and 2:1 cross-section aspect ratio is considered and the fields are presented at 14 GHz in all cases.

Fig 2(a) and 2(b) show a waveguide core of 4.5 mm x 9 mm cross-section with permittivities of 4.85 and 10.2, respectively, and an air cladding. Increasing the core permittivity decreases the waveguide cutoff frequency and increases the extent of field confinement, similar to a dielectric slab waveguide. In this example, the fundamental mode cutoff frequency decreases from 7.9 GHz to 6.3 GHz and the normalized propagation constant P^2 increases from 0.27 to 0.57 at 14 GHz.

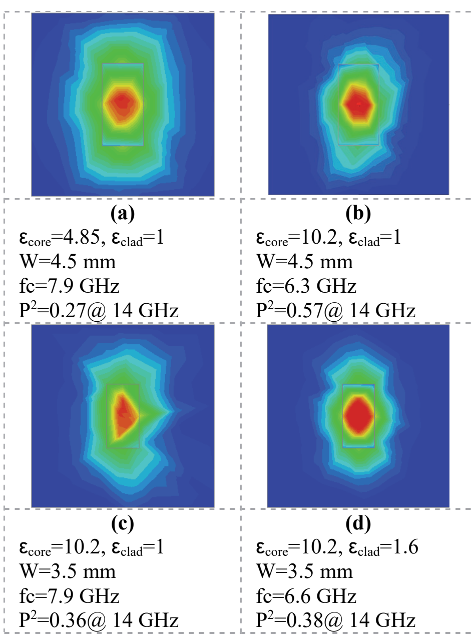

Fig.2. Electric field magnitude of the fundamental mode for DRW designs with different core and cladding permittivities at 14 GHz.

Increasing the core permittivity can result in miniaturized core dimensions. Fig. 2(a) and 2(c) illustrate two DRWs with permittivities of 4.85 and 10.2, respectively, and air cladding that are designed for the same cutoff frequency of 7.9 GHz. It is shown that the high permittivity core width is reduced by 1 mm leading to a 39.5% area reduction. A mathematical relationship between the cutoff frequency, the core permittivity and core width is presented in Section III.

A dielectric cladding can be used to decrease the waveguide cutoff frequency and it could be selected to improve the field confinement. Fig. 2(c) and 2(d) show the same high permittivity core surrounded by air and by an infinite cladding with a permittivity of 1.6, respectively. It is observed that the added cladding decreases the cutoff frequency by 1.3 GHz and increases the field confinement at 14 GHz according to (3).

In this work, a rectangular cross section with a height (H) to width (W) ratio of 2:1 is used in DRW designs to maintain single polarization operation and to avoid field degeneracies [6, 19]. The materials used for simulation and fabrication of the high permittivity core and the cladding are Rogers RO3010 (ε_r=10.2 and loss tangent=0.0035 @ 9 GHz) and ABS (ε_r=2.6 and loss tangent=0.0052 @ 9 GHz), respectively. The MDRW core was optimized in HFSS for the Ku band and the resulting dimensions are W=2.5 mm and H=5 mm. The core dimensions were selected to readily demonstrate the effect of the cladding at the low end of the Ku band. The baseline cladding cross-section area was selected to be a square of 10 mm by 10 mm.

B. *Modal analysis*

As discussed in the previous section, the fundamental mode in a dielectric rod waveguide is E_{11}, for which most of the electric field is propagated through the center of the waveguide core. Fig. 3(a) depicts the E- and H-field vectors of the fundamental mode in a DRW with an air cladding and an aspect ratio of 2:1. Fig 3(b) and (c) show the E-field magnitude of the fundamental mode E^y_{11} in the core cross-section and E-field vectors, respectively. The E-field magnitude and vectors of the first three higher order modes are shown in Fig. 4(a). Fig. 4(b) illustrates the E-field magnitudes for the other higher order mode configurations that the DRW can support.

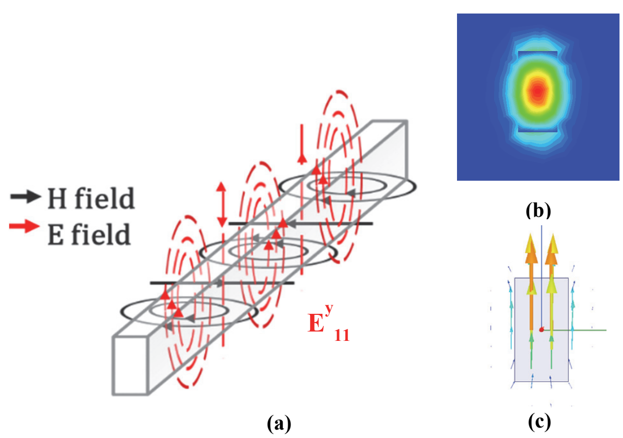

Fig.3. (a) DRW fundamental mode E and H field vectors. (b) E^y_{11} field magnitude and (c) E^y_{11} field vector in the core cross-section.

The only dielectric waveguide geometries that possess exact analytical solutions to guided wave problems are the slab, circular cylinder and the elliptical cylinder waveguides. There is no exact solution to the propagation characteristics of a wave traveling along a rectangular dielectric guide or other cross-sectional geometries. The propagation characteristics for DRW with rectangular cross sections must be found either numerically or by using approximate methods.

Even numerical computation of the fields in rectangular dielectric waveguides can be challenging due to the behavior of the fields in the waveguide corners and the nature of the boundary conditions. The transverse field components are known to be discontinuous and to diverge in the corners, especially for high refractive index ratios between the core and cladding, which might lead to slow convergence when using numerical methods [21].

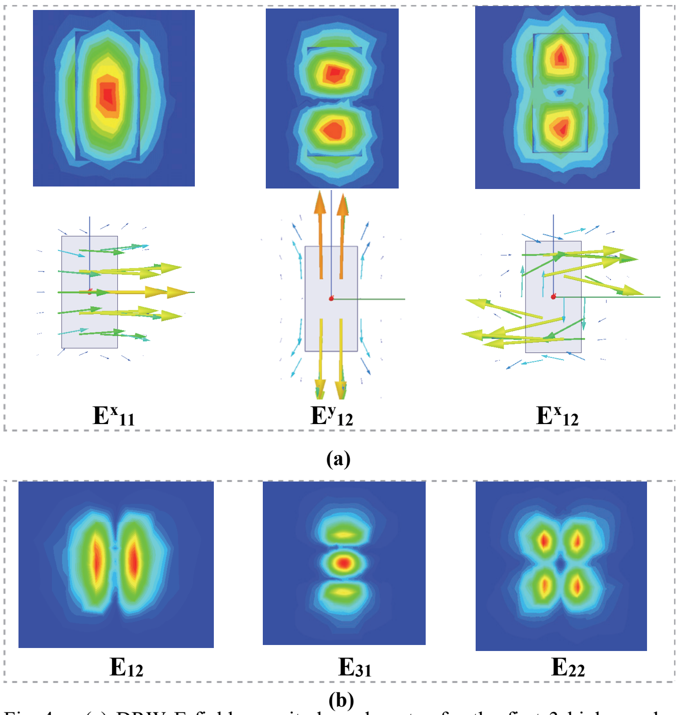

Fig. 4. (a) DRW E-field magnitude and vector for the first 3 higher order modes and (b) other common higher order modes.

Fig. 5 presents the normalized phase constant of the fundamental mode and the first three higher order modes of the DRW and MDRW simulated using Ansys HFSS. The width and height of the core are 2.5 mm and 5.0 mm, corresponding to an aspect ratio of 2:1. The results are presented for the DRW (air cladding) in Fig. 5(a) and for the MDRW (ABS cladding) in Fig. 5(b). The calculated phase constant using Marcatili's explicit approximation is also plotted in Fig. 5 for comparison.

In Marcatili's approximation, the axial propagation constant β or K_z is given by

$$K_z = \sqrt{{K_{core}}^2 - {K_x}^2 - {K_y}^2}, \tag{4}$$

where K_x and K_y are the transverse propagation constants along x and y axis, respectively, and K_{core} is the propagation constant of a plane wave in a medium of refractive index n_{core} [17]. The mathematical expression of K_{core} is:

$$K_{core} = K_0\, n_{core} = (2\pi/\lambda_0)\, n_{core} \tag{5}$$

where λ_0 is the free space wavelength.

For E^y_{mn} and E^x_{mn} modes the transverse propagation constants are given by [17]:

$$K_x = \frac{m\pi}{W}\left(1+\frac{2A}{\pi W}\right)^{-1}, K_y = \frac{n\pi}{H}\left(1+\frac{2A}{\pi H}\frac{n_{clad}^2}{n_{core}^2}\right)^{-1} \tag{6}$$

$$K_x = \frac{m\pi}{W}\left(1+\frac{2A}{\pi W}\frac{n_{clad}^2}{n_{core}^2}\right)^{-1}, K_y = \frac{n\pi}{H}\left(1+\frac{2A}{\pi H}\right)^{-1} \tag{7}$$

where A is the maximum thickness for which an equivalent slab waveguide supports only the fundamental mode, or the maximum thickness in (1).

It is important to mention that the normalized phase constant for a DRW changes from 1, which corresponds to the refractive index of air, to the refractive index of RO3010 when the mode is totally confined as seen in Fig. 5(a). While as shown in Fig. 5(b), the normalized phase constant for a MDRW varies from the refractive index of ABS at the cutoff to the refractive index of RO3010, since the core of a MDRW is surrounded by an infinite homogeneous ABS cladding.

Fig. 5 shows fairly good agreement, well above the cutoff frequencies, between the EM simulation results and Marcatili's approximation for the DRW and MDRW modes. The largest discrepancy occurs near the cutoff frequency for each mode due to the limited accuracy of the Marcatili's approximation assumptions.

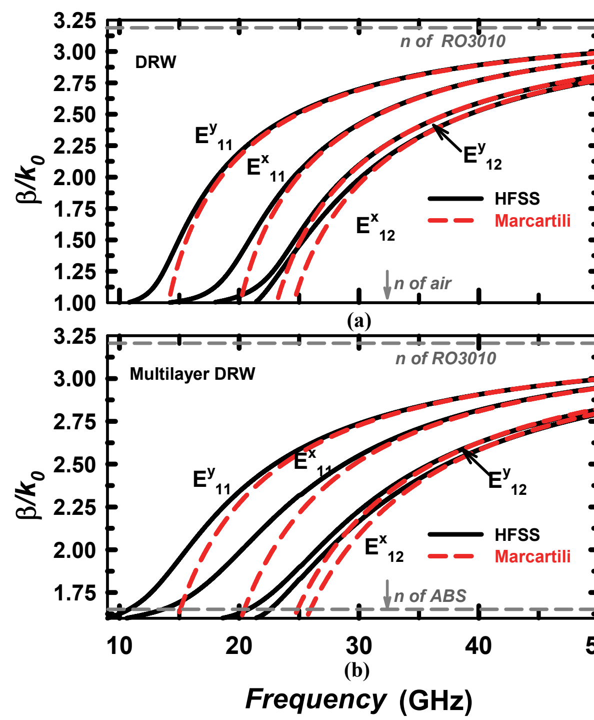

Fig.5. (a) Dielectric rod waveguide normalized phase constants for the first 4 modes using Marcatili's explicit approximation and numerical simulation, considering a DRW, and (b) a MDRW with designs detailed above.

Guided modes in the MDRW vary sinusoidally inside the core and decay exponentially in the cladding. To obtain a closed form solution, Marcatili assumes: a) well-guided modes, which means that most of the electric field is confined inside the core; b) the field strength in the areas on the core corners is negligible; and c) the refractive index of the core is slightly larger than the cladding so that the largest field components are normal to the propagation direction [17]. This derivation was realized in the Cartesian coordinate system by considering a dielectric rod waveguide as a structure formed by two dielectric slab waveguides perpendicular to each other. These assumptions explain the discrepancies in the normalized phase constants for all modes shown in Fig. 5, as well-confined modes do not occur near their cutoff frequencies but rather the field confinement of each mode improves as the frequency increases.

III. Model for the Cutoff Frequency of the MDRW

In this section, a closed-form model is proposed to calculate the cutoff frequency of the fundamental mode in a MDRW of 2:1 aspect ratio. Fig. 6 presents the cutoff frequency of the waveguide for different values of core permittivity and core widths, assuming an air cladding. The MDRW designs with a cladding of varied permittivity for a particular core permittivity are presented in Fig. 7. Fig. 7(a) and 7(b) illustrate the cases for core permittivity of 10.2 and 15, respectively. In both cases the cladding permittivity was varied from 1 to 3.6. All simulations assume an infinite homogeneous cladding and lossless materials used for the core and cladding. The values shown in Fig. 6 and 7 were obtained with full-wave EM simulations using Ansys HFSS. A mathematical fit was performed to the data using the Levenberg–Marquardt algorithm. The resulting model equation is expressed as:

$$f_c = \frac{K\,c}{W^{0.86}\left(2\,\varepsilon_{core}^{0.5} + 3.58\,\varepsilon_{clad}\right)} \tag{8}$$

where W is the core width, c is the speed of light in vacuum and K is given by:

$$K = 1 - 0.455\varepsilon_{clad} + 0.24\varepsilon_{clad}^2 - 0.03\varepsilon_{clad}^3 \tag{9}$$

The model equation is an adaptation of the dielectric slab waveguide expression for the dielectric rod. Rather than being physics-based, the proposed model is a mathematical-based closed-form representation of the EM simulated data. The model was derived under the assumptions mentioned above and for the permittivity values within the range shown in Fig. 6 and Fig. 7.

The model playback shows excellent agreement with the simulated data. As shown in Fig. 6, increasing the core permittivity allows a reduction in the required core dimensions for the same cutoff frequency as expected. Increasing the permittivity of the cladding also allows the core dimensions to be reduced, as shown in Fig. 7. For instance, increasing the cladding permittivity from 1 (air) to 2.6 (ABS) can decrease the cutoff frequency by 24.6% considering the same core size.

As mentioned previously, the model assumes a MDRW core immersed in an infinite cladding. In order to evaluate the effect of the cladding dimension on the fundamental mode cut-off frequency, the normalized phase constant as a function of cladding size is simulated. The cladding considered is formed of ABS and surrounds the waveguide core with a thickness t_{clad}. The cut-off frequency is determined by the intersection of the normalized β curves with the η dashed line, as shown in Fig. 8. The effective refractive index of the cladding ranges between the η of air and the η of ABS due to the variation of the cladding thickness. The results indicate that the model predictions are accurate for claddings much larger than the core size, while offering a good estimation of the cut-off frequency even for thinner claddings. A variation of 1.45 GHz is observed when the cladding thickness is swept from 0 to 40 mm. It is worth mentioning that the cut-off frequency variation becomes progressively less significant as the cladding dimension increases, as shown in Fig. 8.

IV. The Cladding Effect on MDRW Performance

In this work, a transition to rectangular waveguide (RWG) is implemented to characterize the MDRW. The transition, depicted in Fig. 9, has the MDRW core partially inserted into the RWG and maintains the same electric field direction in both waveguides. The inserted MDRW core terminations are tapered to gradually match the impedance and to improve the coupling between the waveguides. In the following sub-sections, the effect of the cladding on the MDRW performance is analyzed and the transition to WR-62 waveguide is considered in the simulations.

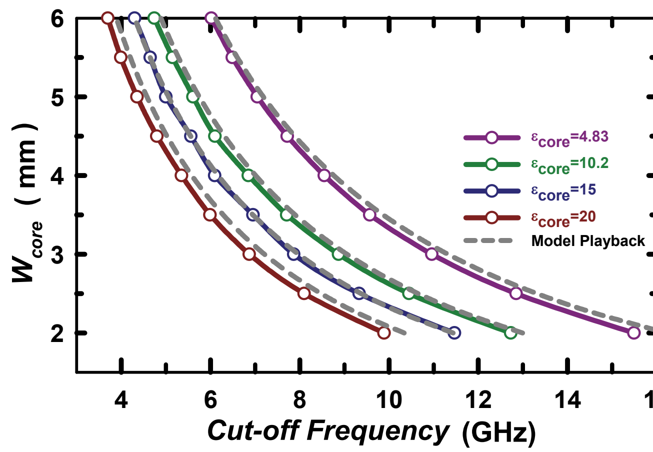

Fig.6. Simulated cutoff frequency of the DRW fundamental mode and proposed model playback considering an air cladding.

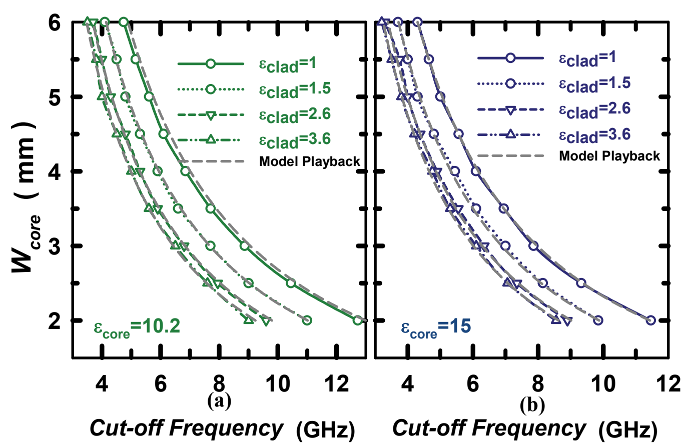

Fig.7. Simulated cutoff frequency of the MDRW fundamental mode and proposed model playback for (a) designs with a core permittivity of 10.2, (a) designs with a core permittivity of 15, both with varied cladding permittivity.

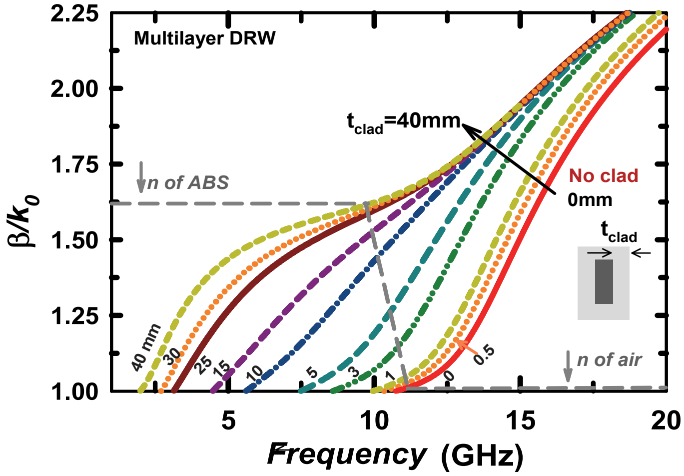

Fig.8. MDRW normalized phase constants for the fundamental mode and a wide range of ABS cladding dimensions.

A. *Loss Tangent Variation*

The effect of the loss tangent (tanδ) is studied in Fig. 10 by considering two cases separately: by varying the cladding loss tangent for lossless as well as Rogers RO3010 cores, and by varying the core loss tangent for lossless as well as ABS claddings. In both cases, the loss tangent is varied from 0 to 0.015. The simulated attenuation data at 14 GHz and 18 GHz are presented in Fig. 10(a) and Fig. 10(b), respectively. Across the frequency band, the attenuation is more sensitive to the core loss tangent than the cladding loss tangent, since most of the electromagnetic field propagates through the core. For the same reason, the difference between the attenuation characteristics for RO3010 and the lossless core (dashed and solid black lines) is larger than the difference between the attenuation responses for ABS and lossless cladding (dashed and solid red lines). This result is observed despite the fact that RO3010 has a lower loss tangent than that of ABS. In addition, the attenuation due to the loss tangent of the core shows a stronger frequency dependence than the attenuation due to the loss tangent of the cladding.

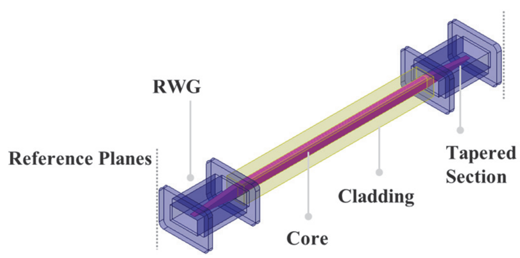

Fig. 9. Schematic diagram showing the transition from a multilayer dielectric rod waveguide to a pair of rectangular waveguides.

B. *Cladding Dimension Variation*

The cladding dimensions also influence the waveguide performance. Fig. 11 shows the 1 dB and 2 dB S_{21} cutoff frequency of the design formed by a Rogers RO3010 core and a square ABS cladding with a varied cross-sectional area. The results correspond to a back-to-back transition from the MDRW to a pair of WR-62 waveguides. The 1 dB and 2 dB cutoff frequencies in this case are calculated as the point where S_{21} reduces by 1 dB and 2 dB from the minimum insertion loss, respectively. The simulated results in Fig. 11 indicate that the optimal cross-section dimensions for this design is 20 mm × 20 mm. As shown previously in Fig. 8, increasing the cladding size of the MDRW reduces the fundamental mode cutoff frequency up to a certain value. For cladding sizes larger than 20x20 mm^2, ripples in S21 and S11 were observed in simulated data. These ripples might indicate that the rectangular metal waveguide feed approach is ineffective and a different transition design may be

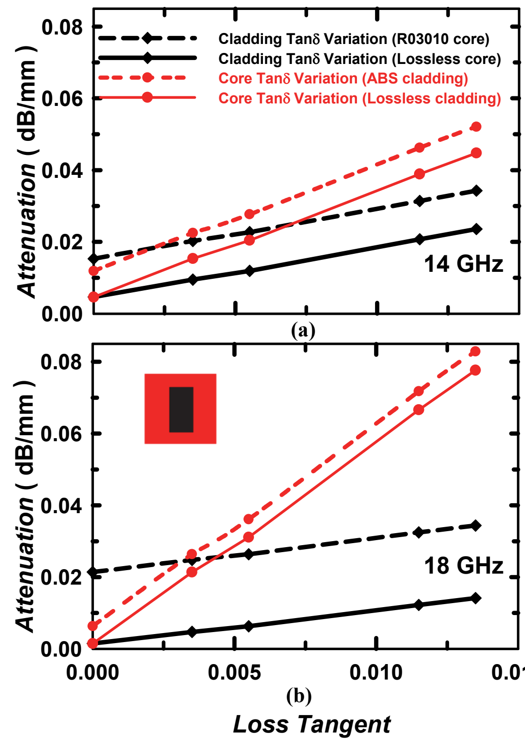

Fig. 10. Simulated attenuation versus loss tangent variation at (a) 14 GHz and (b) 18 GHz.

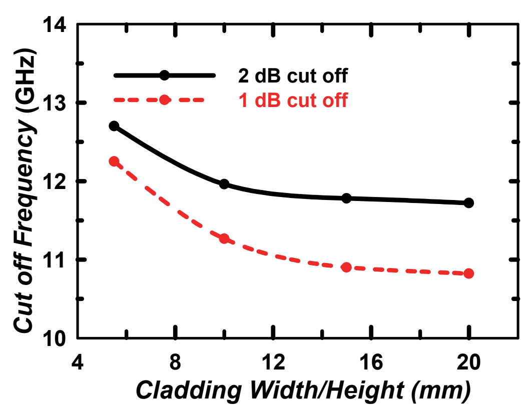

Fig. 11. Simulated 1 dB and 2 dB cutoff frequency for a MDRW with W=2.5 mm and H=5 mm versus cladding width/height with square cross sections.

C. *Cladding Permittivity Variation*

Fig. 12 presents the 1 dB and 2 dB S_{21} cutoff frequencies of the design formed by a Rogers RO3010 core and a 10 × 10 mm^2 cladding with a relative permittivity varied from 1 to 5.5. As the cladding permittivity increases from 1, the waveguide cut off frequency decreases while gradually reaching a minimum value. This result agrees with those presented in Fig. 7, in which the curves of W_{core} versus cutoff frequency approach each other as the cladding permittivity increases. In this case, the optimal values for permittivity lie around 4.6, since a substantial decrease in cutoff frequency for extended bandwidth is observed.

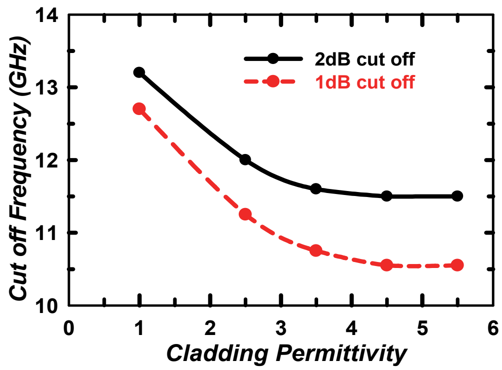

Fig. 12. Simulated 1 dB and 2 dB cutoff frequencies versus cladding permittivity.

V. MDRW Experimental Characterization

A. Characterization of Straight DRW and MDRW

The performance of the MDRW was measured with a transition to a pair of standard WR-62 rectangular waveguides as shown in Fig. 9. The dimensions of the design are presented in Fig. 13(a). The length of the tapered section at each port was optimized by Ansys HFSS 3D EM simulation using a parametric sweep. This type of tapered transition to RWG has been effectively implemented at the W, D and F bands using sapphire and silicon waveguides [6, 19, 22].

A picture of the fabricated multilayer waveguide is shown in Fig. 13(b). The RO3010 waveguide core was cut into shape using a Rabbit HX-1290SE laser cutter. A 10x10 mm^2 and 20x20 mm^2 cladding were manufactured as a hollow structure by fused deposition modeling of ABS with 100% infill and 150 µm layer thickness using a tabletop nScrypt 3D printer. A 50 micron-thick layer of Rogers Ultralam 3850 liquid crystal polymer (LCP) (ε_r=3.14, tanδ=0.002 at 10 GHz) was patterned and attached to the WR-62 flange to align and hold the MDRW core at the center of the RWG aperture. The performance of this waveguide with and without a 10x10 mm^2 cladding is presented in [13].

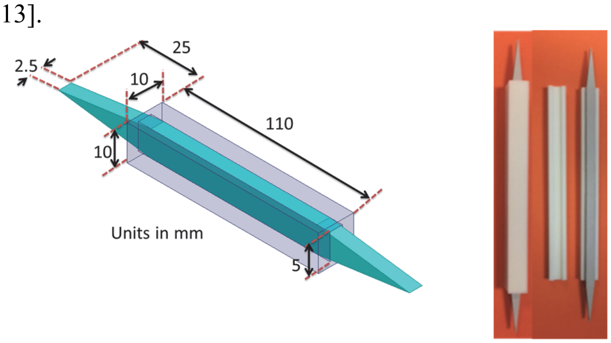

(a) (b)

Fig. 13. Schematic diagram of the 2-port measurement setup showing the transition from multilayer dielectric rod waveguide to rectangular waveguide by showing (a) the key dimensions, and (b) fabricated MDRWs.

The measured and simulated data of the DRW and MDRW with a 10 × 10 mm^2 ABS cladding are shown in Fig. 14(a) and (b), respectively. These results include the effects of back-to-back transitions to RWG. The MDRW exhibits a reduction of the 1 dB and 2 dB cutoff frequencies by 1 GHz and 1.9 GHz, respectively, when compared to the DRW without cladding. A total attenuation between 0.019 and 0.04 dB/mm is achieved over the extended Ku-band. The simulated and measured data for a MDRW design with a 20 × 20 mm^2 cladding is presented in Fig. 14(c), showing even greater improvement in the waveguide performance at low frequencies. Discrepancies between the measured and simulated data can be largely ascribed to misalignments of the waveguides during measurement.

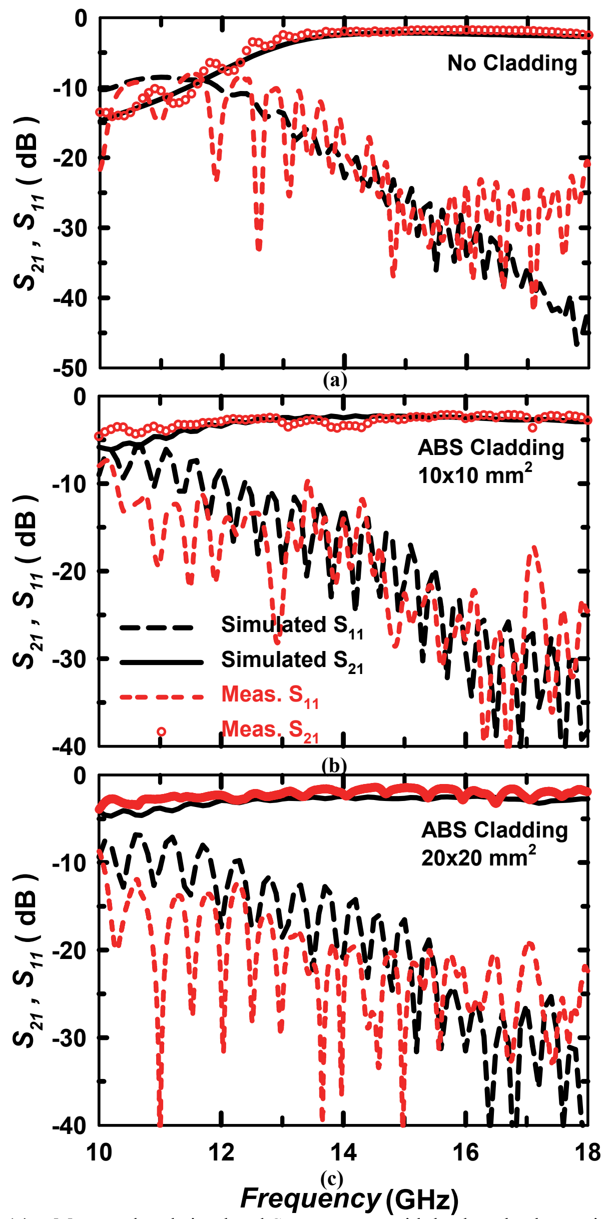

Fig. 14. Measured and simulated S parameters with back-to-back transitions to RWG for (a) a DRW without cladding [13], (b) a MDRW with 10×10 mm^2 ABS cladding [13], and (c) a MDRW with 20×20 mm^2 ABS cladding.

The presence of the cladding has minimal impact on the

MDRW insertion loss at higher frequencies since most of the electric field is concentrated in the waveguide core. The high frequency attenuation is thus comparable to the attenuation of a plane wave propagating in an infinite, uniform medium of the same material as the core. The attenuation of a plane wave is given by [23]

$$\alpha = \omega\sqrt{\mu\varepsilon}\left\{\frac{1}{2}\left[\sqrt{1+\left(\frac{\sigma}{\omega\varepsilon}\right)^2}-1\right]\right\}^{1/2}; \quad (10)$$

for low loss dielectric it can be approximated to

$$\alpha \approx \frac{\sigma}{2}\sqrt{\frac{\mu}{\varepsilon}}, \quad (11)$$

where $\sigma = tan\delta\omega\varepsilon$. Using the properties of RO3010, (11) yields 0.018dB/mm at 18 GHz.

B. Characterization of DRW and MDRW Bends

Fig. 15 shows the performance of a DRW without cladding and a MDRW with a 10 × 10 mm² ABS cladding, which both contain a 35 mm-long 90° radius of curvature bend. The tested results show that the MDRW bends have an extended operational bandwidth at the lower end of the frequency band, similar to the straight waveguides. The MDRW bend shows a reduction of the 1 dB cutoff frequency and the 2 dB cutoff frequency both by 1.6 GHz when compared to the DRW bend. As previously discussed, the effect of the cladding is significant at low frequencies, while the attenuation with and without the cladding is approximately the same at frequencies above 15 GHz.

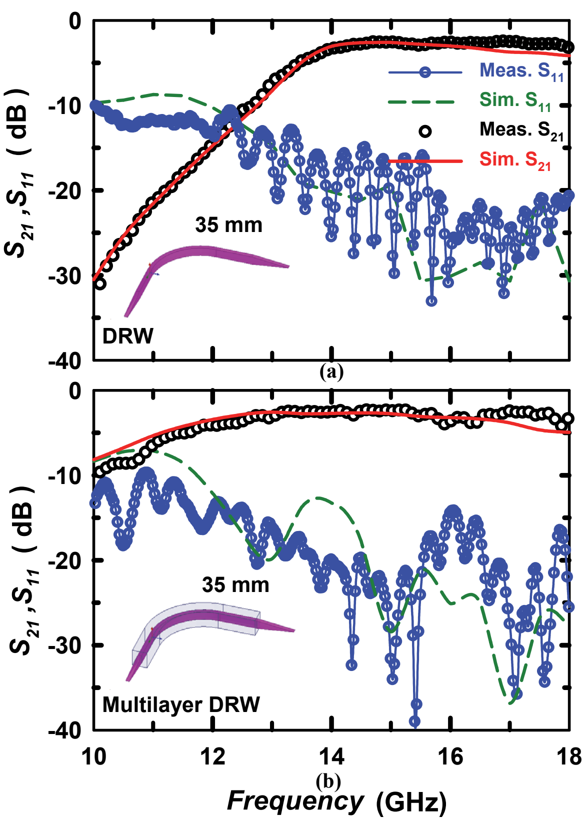

Fig. 15. Measured and simulated S-parameters of (a) a DRW without cladding, and (b) a MDRW with 10 × 10 mm² ABS cladding, both with a 35 mm radius 90° bend.

Fig. 16 shows the measured 1 dB cut off frequency of DRW bends with different radius of curvature for a DRW and a MDRW with a 10×10 mm² ABS cladding. As the radius of curvature decreases, a higher portion of the E-field is radiated at the DRW bend resulting in higher attenuation and higher 1 dB cutoff frequencies. For larger radius of curvature, the 1 dB cut off frequency gets closer to the value for the straight waveguide (infinite radius of curvature). As shown in Fig. 16, the multilayer DRW bend shows an extended bandwidth ranging from 1 to 1.6 GHz when compared to a single layer bend.

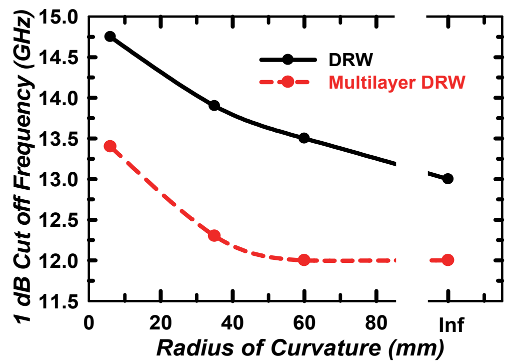

Fig. 16. Comparison of measured 1 dB cut off frequency versus radius of curvature of a DRW and a MDRW.

C. Loss Analysis for the MDRW

The total attenuation of the MDRW depends on the transition to RWG, the total length of the waveguide and the material properties of the core and cladding. The waveguide attenuation can be isolated from the attenuation due to the transitions by applying the multiline method [6, 24, 25]. This numerical calibration method is used to remove the effect of the transitions at each port from the uncalibrated S parameters. The cascade or transmission parameters of the entire system $[T_t]$ can be written as the multiplication of the matrices of each transition $[T_{trans}]$ to RWG at both ports and the characteristic matrix of the DRW or MDRW $[T_{DRW}]$ as shown in (12).

$$[T_t]^i = [T_{trans1}]\cdot[T_{DRW}]^i\cdot[T_{trans2}], \quad (12)$$

where the index i denotes the length of the MDRW. The transmission matrix of the entire system can be directly determined from the measured S parameters.

Assuming that the MDRW is an ideal transmission line, its transmission parameters are given by:

$$[T_{DRW}]^i = \begin{bmatrix} e^{-\gamma li} & 0 \\ 0 & e^{\gamma li} \end{bmatrix}, \quad (13)$$

where γ is the propagation constant and li is the physical length of the line.

Considering two dielectric rod waveguides of different lengths $L=li$ *and* $L=lj$, with otherwise identical design parameters, (12) can be rewritten as follows:

$$[T_t]^{ij}\cdot[T_{trans1}] = [T_{trans1}]\cdot[T_{DRW}]^{ij}, \quad (14)$$

where

$$[T_t]^{ij} = [T_t]^j\cdot[T_t]^{i^{-1}}, \quad (15)$$

and

$$[T_{DRW}]^{ij} = [T_{DRW}]^{j} \cdot [T_{DRW}]^{i^{-1}} = \begin{bmatrix} e^{-\gamma(lj-li)} & 0 \\ 0 & e^{\gamma(lj-li)} \end{bmatrix} \quad (16)$$

The eigenvalues of $[T_t]^{ij}$ can be calculated from the combined system transmission matrix and these can be equated to the eigenvalues of $[T_{DRW}]^{ij}$. Since $[T_{DRW}]^{ij}$ is a diagonal matrix, its eigenvalues are the diagonal elements. Consequently, the propagation constant of the transmission line can be determined as:

$$\gamma = \frac{ln(\lambda_t^{ij})}{li-lj} \ , \quad (17)$$

where λ_t^{ij} is the average of both eigenvalues of $[T_{DRW}]^{ij}$. Therefore, the total attenuation of the MDRW can be calculated as:

$$\alpha_{Total} = Re\{\gamma\} \ . \quad (18)$$

The attenuation due to radiation can be calculated with (18) by repeating the multiline method this time with lossless waveguides. Finally, the attenuation due to the dielectric losses can be determined by subtracting the attenuation due to radiation from the total attenuation:

$$\alpha_{Dielectric} = \alpha_{Total} - \alpha_{Radiation} \ . \quad (19)$$

Fig. 17(a) and (b) present the resulting attenuation per unit length due to the dielectric losses ($\alpha_{Dielectric}$) and radiation ($\alpha_{Radiation}$) as well as the total attenuation (α_{Total}) for the DRW and the MDRW with a 10 × 10 mm^2 ABS cladding, respectively. The total attenuation values shown in Fig. 17 are calculated based on simulated and measured data of 110 mm and 200 mm long waveguides. The values for $\alpha_{Radiation}$ are calculated with simulated data, since it considers lossless waveguides of different lengths, as previously mentioned. Considering this result and the simulated α_{Total}, $\alpha_{Dielectric}$ is determined through eq. (19). The simulated curves show that the addition of the cladding reduces the total attenuation at lower frequencies without a significant increase in the attenuation at higher frequencies. In both cases, the maximum simulated $\alpha_{Dielectric}$ is ~0.023 dB/mm; it increases with frequency since a higher portion of the E-field travels through the dielectric, and is close to the attenuation of a plane wave as calculated in section V.A (~0.018 dB/mm). The simulated $\alpha_{Radiation}$ is very low for the MDRW in the entire frequency range and above 14 GHz for the DRW. The average simulated $\alpha_{Radiation}$ above 14 GHz in both cases is ~7x10^{-4} dB/mm. The total attenuation calculated with measured data shows a wide variation, between ~0.05-0.03 dB/mm for DRW and ~0.05-0.035 dB/mm for MDRW. This variation is due to ripples in the measured data, although the curve fluctuates about the data predicted through the simulations.

The total attenuation shown in Fig. 17 is lower than the insertion loss of the same waveguides presented in Fig. 14, since the effects of the transition to RWG and impedance mismatch have been removed. The additional loss can be accurately estimated above 14 GHz where both the MDRW and DRW have negligible radiation losses based on EM simulations. To determine the attenuation due to the transition, a simulation with lossless transition sections was performed and compared to its lossy counterpart. The resulting loss was estimated to be <0.2 dB per transition between 14-18 GHz for both MDRW and DRW waveguides. The remaining simulated attenuation can be attributed to impedance mismatch, which is <0.5 dB between 14-18 GHz. It is worth mentioning that the DRW and MDRW allow multimode transmission in the considered frequency range, as shown in Fig. 5. Nevertheless, the transition from the WR-62 waveguide only excites the fundamental mode up to 18 GHz and for this reason the losses due to multimode propagation have not been considered in the analysis.

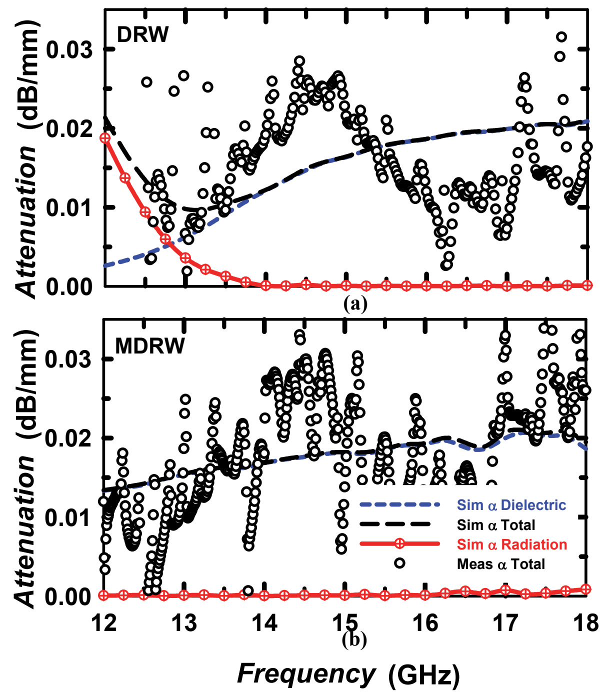

Fig. 17. Attenuation due to radiation and dielectric losses as well as the total attenuation calculated from simulated and measured data for (a) a DRW with W=2.5 mm and H=5.0 mm, and (b) an identically sized MDRW with a 10 × 10 mm^2 ABS cladding.

VI. Conclusion

The design and performance of a multilayer dielectric rod waveguide with a rectangular cross section and a 2:1 core cross-section aspect ratio (W=2.5 mm and H=5.0 mm) has been studied across the extended Ku band (10 to 18 GHz). A mathematical model is presented to predict the fundamental mode cutoff frequency of the MDRW as a function of the material properties and core dimensions. The model is an adaptation of the dielectric slab waveguide cutoff frequency expression for the dielectric rod and it aims to: 1) reduce the extensive simulation time in the design stage that results from full-wave EM simulations, and 2) provide insights into the relationship between the key design parameters.

The performance of the MDRW is proven to be superior as compared to its single layer counterpart. The multilayer waveguides show a 16.7% and 24% bandwidth extension due to lowered 1 dB cutoff frequency for designs with 10 × 10 mm^2

and 20 × 20 mm^2 cladding areas, respectively. It also shows significant insertion loss improvements in the lower end of the band for 90-degree waveguide bends. The performance of DRW and MDRW bends of 6 mm, 35 mm and 60 mm radius of curvature was measured. MDRW bends show a bandwidth extension between 1 GHz and 1.6 GHz when compared to a single-layer dielectric rod waveguide bend of the same curvature and same core dimensions. The corresponding attenuation due to the MDRW configuration and due to each transition to RWG were extracted using a numerical calibration method. The resulting values show a maximum attenuation of ~0.023 dB/mm due to the dielectric losses, an attenuation due to each RWG transition between 0.2 dB and 0.55 dB, and an attenuation due to radiation losses of about $7x10^{-4}$ dB/mm.

ACKNOWLEDGMENT

The authors wish to acknowledge the assistance and support of Rogers Corporation, Sciperio, Inc. and Ramiro Ramirez.

REFERENCES

[1] M. Nitas, V. Salonikios, S. Raptis, and T. V. Yioultsis, "Analysis and design of fully planar CSRR-enhanced substrate-integrated waveguides and slot antennas for 5G communications," in *2018 7th International Conference on Modern Circuits and Systems Technologies (MOCAST)*, 2018, pp. 1-5.

[2] O. Mitrofanov, R. James, F. A. Fernandez, T. K. Mavrogordatos, and J. A. Harrington, "Reducing Transmission Losses in Hollow THz Waveguides," *IEEE Transactions on Terahertz Science and Technology,* vol. 1, pp. 124-132, 2011.

[3] F. Töpfer, S. Dudorov, and J. Oberhammer, "Millimeter-Wave Near-Field Probe Designed for High-Resolution Skin Cancer Diagnosis," *IEEE Transactions on Microwave Theory and Techniques,* vol. 63, pp. 2050-2059, 2015.

[4] S. Atakaramians, S. Afshar V, T. M. Monro, and D. Abbott, "Terahertz dielectric waveguides," *Advances in Optics and Photonics,* vol. 5, pp. 169-215, 2013/06/30 2013.

[5] Q. Zhong, Z. Chen, N. Sharma, S. Kshattry, W. Choi, and K. O. Kenneth, "300-GHz CMOS QPSK transmitter for 30-Gbps dielectric waveguide communication," in *2018 IEEE Custom Integrated Circuits Conference (CICC)*, 2018, pp. 1-4.

[6] A. Malekabadi, S. A. Charlebois, D. Deslandes, and F. Boone, "High-Resistivity Silicon Dielectric Ribbon Waveguide for Single-Mode Low-Loss Propagation at F/G-Bands," *IEEE Transactions on Terahertz Science and Technology,* vol. 4, pp. 447-453, July 2014.

[7] H. Kogelnik, "Theory of Dielectric Waveguides," in *Integrated Optics*, T. Tamir, Ed., ed Berlin, Heidelberg: Springer Berlin Heidelberg, 1975, pp. 13-81.

[8] C. R. Doerr and H. Kogelnik, "Dielectric Waveguide Theory," *Journal of Lightwave Technology,* vol. 26, pp. 1176-1187, 2008.

[9] S. Atakaramians, S. Afshar V., B. M. Fischer, D. Abbott, and T. M. Monro, "Porous fibers: a novel approach to low loss THz waveguides," *Optics Express,* vol. 16, pp. 8845-8854, 2008.

[10] S. Atakaramians, S. Afshar V., H. Ebendorff-Heidepriem, M. Nagel, B. M. Fischer, D. Abbott*, et al.*, "THz porous fibers: design, fabrication and experimental characterization," *Optics Express,* vol. 17, pp. 14053-14062, 2009/08/03 2009.

[11] J. C. Myers, J. A. Hejase, J. Tang, and D. M. Dreps, "Embeded filtering in PCB integrated ultra high speed dielectric waveguides using photonic band gap structures," in *2017 IEEE 26th Conference on Electrical Performance of Electronic Packaging and Systems (EPEPS)*, 2017, pp. 1-3.

[12] X. Yang and P. P. Chahal, "On-Wafer Terahertz Ribbon Waveguides Using Polymer-Ceramic Nanocomposites," *IEEE Transactions on Components, Packaging and Manufacturing Technology,* vol. 5, pp. 245-255, 2015.

[13] D. Lugo, R. A. Ramirez, J. Wang, and T. Weller, "Low Permittivity Cladding to Improve the Performance of Dielectric Rod Waveguides and Dielectric End-Fire Antennas," presented at the 2016 IEEE MTT-S International Microwave Symposium, San Francisco, CA, 2016.

[14] T. P. Ketterl, Y. Vega, N. C. Arnal, J. W. I. Stratton, E. A. Rojas-Nastrucci, C. M. F*, et al.*, "A 2.45 GHz Phased Array Antenna Unit Cell Fabricated Using 3-D Multi-Layer Direct Digital Manufacturing," *IEEE Transactions on Microwave Theory and Techniques,* vol. 63, pp. 4382-4394, 2015.

[15] E. A. Rojas-Nastrucci, T. Weller, V. Lopez Aida, C. Fan, and J. Papapolymerou, "A study on 3D-printed coplanar waveguide with meshed and finite ground planes," in *Wireless and Microwave Technology Conference (WAMICON), 2014 IEEE 15th Annual*, 2014, pp. 1-3.

[16] D. C. Lugo, R. A. Ramirez, J. Castro, J. Wang, and T. M. Weller, "Ku-band additive manufactured multilayer dielectric rod waveguide," presented at the 2017 IEEE 18th Wireless and Microwave Technology Conference (WAMICON), Cocoa Beach, FL, 2017.

[17] E. A. J. Marcatili, "Dielectric Rectangular Waveguide and Directional Coupler for Integrated Optics," *Bell System Technical Journal,* vol. 48, pp. 2071-2102, 1969.

[18] J. E. Goell, "A circular-harmonic computer analysis of rectangular dielectric waveguides," *The Bell System Technical Journal,* vol. 48, pp. 2133-2160, Sept. 1969.

[19] S. Dudorov, "Rectangular Dielectric Waveguide and its Optimal Transition to a Metal Waveguide," Helsinki University of Technology, 2002.

[20] C. Yeh and F. Shimabukuro, *The Essence of Dielectric Waveguides*, 2008.

[21] A. S. Sudbo, "Why are accurate computations of mode fields in rectangular dielectric waveguides difficult?," *Journal of Lightwave Technology,* vol. 10, pp. 418-419, 1992.

[22] N. Ranjkesh, M. Basha, A. Taeb, A. Zandieh, S. Gigoyan, and S. Safavi-Naeini, "Silicon-on-Glass Dielectric Waveguide—Part I: For Millimeter-Wave Integrated Circuits," *IEEE Transactions on Terahertz Science and Technology,* vol. 5, pp. 268-279, 2015.

[23] D. M. Pozar, *Microwave engineering*: Fourth edition. Hoboken, NJ : Wiley, 2012.

[24] R. B. Marks, "A multiline method of network analyzer calibration," *IEEE Transactions on Microwave Theory and Techniques,* vol. 39, pp. 1205-1215, 1991.

[25] M. D. Janezic and J. A. Jargon, "Complex permittivity determination from propagation constant measurements," *IEEE Microwave and Guided Wave Letters,* vol. 9, pp. 76-78, Feb 1999.

Denise C. Lugo (S'11-M'18) She received the Professional Electronics Engineer degree in 2009 and the Magister of Electronics Engineering degree, with a major in Solid State Electronics, in 2011, both from Simón Bolívar University, Caracas, Venezuela. She later received her M.S. and Ph.D. in electrical engineering from University of South Florida in 2015 and 2018 respectively. Her Ph.D. research was focused on the design of millimeter-wave 3D printed dielectric waveguides for sensing applications. She is now with Qorvo, inc.

Jing Wang (S'02–M'06) received the dual B.S. degrees in mechanical engineering and electrical engineering from Tsinghua University, Beijing, China, in 1994, and the dual M.S. degrees in electrical engineering and mechanical engineering and the Ph.D. degree in electrical engineering from the University of Michigan, Ann Arbor, in 2000, 2002, and 2006, respectively.

He joined the University of South Florida, in 2006, where he is currently Professor with the Electrical Engineering Department. His current research interests include RF/Microwave/ devices, advanced additive manufacturing, micromachined transducers, energy scavengers, functional nanomaterials, microfluidics, flexible/RF/microwave electronics, MMICs, and wireless sensors. He has authored or coauthored over 140 professional journal and conference publications and he holds eleven U.S. patents.

Thomas M. Weller (S'92–M'95–SM'98-F'18) received the B.S., M.S., and Ph.D. degrees in electrical engineering from the University of Michigan, Ann Arbor, in 1988, 1991, and 1995, respectively. From 1988 to 1990, he was with Hughes Aircraft Company, El Segundo, CA, USA. He was with the Electrical Engineering Department at the University of South Florida from 1995 – 2018. He joined Oregon State University in 2018, where he is currently the Michael and Judith Gaulke Professor and School Head in Electrical Engineering and Computer Science. He co-founded Modelithics, Inc., in 2001. He was a recipient of the Outstanding Young Engineer Award from the IEEE Microwave Theory and Techniques Society in 2005, the USF President's Award for Faculty Excellence in 2003, the IBM Faculty Partnership Awards in 2000/2001, a National Science Foundation CAREER Award in 1999, and the IEEE MTT Society Microwave Prize in 1996. He has 37 U.S. patents and over 300 professional journal and conference publications. His current research interests are in the areas of additive manufacturing, development and application of microwave materials, and integrated circuit and antenna design.